A Time-Resolved Dynamic Stall Investigation Based on Coherent Structure Analysis

Karen Mulleners[1] **and Markus Raffel**[2]

1: German Aerospace Centre (DLR), Göttingen, Germany, karen.mulleners@dlr.de
2: German Aerospace Centre (DLR), Göttingen, Germany, markus.raffel@dlr.de

Abstract Dynamic stall on an airfoil comprises a series of complex aerodynamic phenomena in response to an unsteady change of the angle of attack. It is accompanied by a lift overshoot and delayed massive flow separation with respect to static stall. The classical hallmark of the dynamic stall phenomenon is the dynamic stall vortex. The flow over an oscillating OA209 airfoil under dynamic stall conditions was investigated by means of unsteady surface pressure measurements and time-resolved particle image velocimetry. The characteristic features of the unsteady flow field were identified and analysed utilising different coherent structure identification methods. An Eulerian and a Lagrangian procedure were adopted to locate the axes of vortices and the edges of Lagrangian coherent structures, respectively. Additionally, the velocity field was subjected to a proper orthogonal decomposition yielding the energetically dominant coherent flow patterns and their temporal evolution. The complementary information obtained by these methods provided deeper insight into the spatiotemporal evolution of vortical structures within a single dynamic stall life cycle. In particular, the onset of dynamic stall, generally defined as the detachment of the primary stall vortex, was specified here based on a characteristic mode of the proper orthogonal decomposition of the velocity field. Variations in the flow field topology that accompany the stall onset were verified by the Lagrangian coherent structure analysis. Furthermore, a subtle but significant change was observed in the orientation of the trajectories of the vortices that originate at the very leading edge shortly before and after stall onset. The mechanism that results in the detachment of the dynamic stall vortex from the airfoil was identified as a vortex induced separation caused by strong viscous interactions.

1 Introduction

The dynamic stall process of the flow over a constantly pitching airfoil comprises a series of complex aerodynamic phenomena and is deemed a prominent example of unsteady separation. It can be recognised by a lift overshoot and a delay in the onset of massive flow separation with respect to static stall. The salient feature of the unsteady separating flow is the formation and convection of a large-scale coherent structure referred to as the dynamic stall vortex. The most prominent example can be observed on the retreating blades of an helicopter rotor in forward flight. However, wind turbines, turbomachinery compressors, highly manoeuvring fixed wing aircraft, etc. are equally affected. Although the dynamic stall delay and the related increase of the maximum lift can be beneficial in some applications, the large excursions of the aerodynamic loads that emerge during vortex break down induce strong vibrations and structural loads, potentially fatal for a helicopter rotor. Hence, due to the incessant interest in improving the manoeuvrability and performance of rotary-wing aircraft and rapidly manoeuvring aircraft, dynamic stall has been the subject of numerous investigations during past decades and continues to be an object of scrutiny (McAlister et al., 1978; McCroskey, 1981; Carr, 1988).

A detailed analysis of the dynamic stall events on an oscillating airfoil was presented by Carr et al. (1977). They revealed that the prominent features within a full cycle of oscillation are consecutively the emergence and spreading of flow reversal on the airfoil's suction side, the formation and convection of a large-scale leading edge vortex, massive flow separation, and finally flow reattachment. Analogously, Shih et al. (1992) classified the unsteady flow development over an airfoil pitching up at constant rate into four successive stages: 1) a vortex formation stage, 2) a vortex convection stage,

3) stall onset, and 4) a stalled stage. Both descriptions show that the flow over either a constantly pitching or oscillating airfoil is qualitatively characterised by the same prominent features, being the initiation, growth and shedding of a leading edge vortex and the associated lift overshoot. For both types of motion the process of vortex formation and convection result in a delay of massive flow separation to angles of attack beyond the static stall angle. During this delay the lift continues to increase with increasing angle of attack yielding the lift overshoot which is characteristic of dynamic stall. The inception of stall is generally accompanied by a loss of lift and an increase of the negative pitching moment and marks the beginning of the stalled stage. This stage can be recognised by large-scale vortex shedding and associated large fluctuations of the lift, drag and pitching moment. Furthermore, when the airfoil motion is oscillatory a large amount of load hysteresis is present.

Although a lot of effort – analytical as well as numerical and experimental – has been devoted in the past to enhance the comprehension of the phenomenology of dynamic stall, it is not yet fully understood and characterised. In particular, the process that leads to the formation of the primary stall vortex and the mechanism that causes the vortex to break contact with the airfoil are still controversial issues requiring further and deeper examination. Advances in the understanding of unsteady separation yield a different and a clearer appreciation of the dynamic stall phenomenon (Van Dommelen and Cowley, 1980; Doligalski et al., 1994; Degani et al., 1998).

Accurate knowledge of the state of the fluid flow during dynamic stall is strongly tied to a fundamental understanding of the development and interaction of coherent structures. Due to the incessant technological progress during the last decades yielding the development of state-of-the-art digital cameras, high repetition rate lasers and sophisticated evaluation algorithms, the PIV technique established itself as a valuable and indispensable tool in experimental fluid dynamics. However, the investigation of vortices and vortex dynamics from experimental data remains a challenging task due to the lack of a universally accepted definition of vortical structures and the difficulty to quantify them. Several specific definitions have been proposed hitherto by i. a. Lugt (1979); Robinson (1991); and Haller (2005). Despite the plethora of publications on the issue no consensus has been reached yet, reflecting the complexity of the subject area. As a direct consequence, unambiguous vortex detection remains elusive and various Eulerian and Lagrangian criteria have been introduced over the years with different validity depending on the specific problem.

Within the scope of this study, the conspicuous features of the experimentally investigated flow over a sinusoidally oscillating airfoil in a uniform flow are identified and analysed utilising a combination of an Eulerian vortex centre allocation procedure (Michard et al., 1997), a Lagrangian approach based on the Lyapunov exponent (Haller and Yuan, 2000), and a proper orthogonal decomposition (POD) of the velocity field (Sirovich, 1987). Whereas past experimental investigations generally involve phase-locked measurements, the present study provides time-resolved recordings of the velocity field in addition to unsteady surface pressure distributions and allows for the examination of the chronology of events during a full cycle of oscillation. The main objective is to combine the complementary information provided by the different vortex identification procedures in order to deliver insight into the spatiotemporal evolution of vortical structures within a single dynamic stall life cycle.

The paper is organised as follows. Prior to the description of the applied coherent structure identification procedures, the experimental details will be specified. Subsequently, the experimental results are presented and discussed. The discussion covers the examination of the chronology of events during an entire dynamic stall life cycle and a detailed analysis of the onset of dynamic stall. The discussion is concluded by a short summary of the most important findings and by suggesting further avenues of investigation.

2 Experimentals

Wind tunnel experiments were conducted to investigate dynamic stall on a constantly pitching airfoil in a uniform flow at a free stream Reynolds number $Re = 9.2 \times 10^5$ based on the chord length c (Mach number $Ma = 0.14$). A two-dimensional airfoil model with an OA209 profile was subjected to a sinusoidal oscillating motion about its quarter chord axis with a mean incidence α_0, an amplitude α_1, and an oscillation frequency f_{osc}. The latter is preferably written in dimensionless form as the reduced frequency $k = \pi f_{\mathrm{osc}} c/U_\infty$, where U_∞ is the free steam velocity. The mean incidence, amplitude and reduced frequency were varied such that $\alpha_0 \in \{18°, 20°, 22°\}$, $\alpha_1 \in \{6°, 8°\}$, and $k \in \{0.050, 0.075, 0.10\}$.

Stereoscopic time-resolved particle image velocity (TR-PIV) measurements were conducted in the cross sectional plane at model mid-span. The width of the field of view covered the entire chord for the relevant angle of attack range. As maximally allowed by the hardware, time series of 6144 frames with full camera resolution were recorded at 3000 Hz, corresponding to an acquisition rate of 1500 Hz for the velocity fields. After mapping the views of both cameras, the dimensions of the PIV measurement window were 335 mm × 165 mm and the spatial resolution of the recording was 5.0 px/mm. The PIV images were processed using an interrogation window size of 32 px × 32 px and an overlap of approximately 80 % yielding a grid spacing of 6 px or 1.2 mm which is less then $0.005\,c$. The interrogation window size was minimised ensuring an acceptable signal-to-noise ratio. The window overlap on the other hand was maximised to avoid artificial smoothing of velocity gradients (Richard et al., 2006). By doing so the spatial resolution of the results of the vortex detection algorithms was improved. Prior to the coherent structure analysis, the velocity fields were rotated into the airfoil reference system with the x-axis along the chord, the y-axis along the span and the z-axis upward perpendicular to the chord, while the origin coincides with the rotation axis, i. e. the airfoil's quarter chord axis, at model mid-span. Simultaneously to the TR-PIV, the surface pressure distribution at the model mid-span was scanned at approximately 6 kHz for about 15 s. The data acquisition was synchronised with the recording of the PIV images allowing for straightforward assignment of the instantaneous pressure distributions and incidence angles to each of the acquired velocity fields.

3 Coherent Structure Analysis

The common goal of coherent structure identification methods is to locate, extract, and visualise conspicuous flow structures characterised by various spatial and temporal scales.

3.1 Eulerian Method

A survey through literature yields a considerable number of Eulerian identification criteria. Eulerian structure detection typically deals with spatial structures of quantities derived from the instantaneous velocity field and its gradients. Comprehensive reviews of the diversity of Eulerian vortex eduction schemes and their applications are provided by Jeong and Hussain (1995) and Cucitore et al. (1999). Among the most cited and commonly used Eulerian vortex detection criteria are the Q-criterion introduced by Hunt et al. (1988), the Δ-criterion of Chong et al. (1990), and the λ-criterion proposed by Jeong and Hussain (1995). In most flow situations these three criteria yield similar structures which correctly represent the topology and geometry of the vortex cores in the Eulerian frame of reference. Nevertheless, they share several disadvantages.

The most inconvenient and inevitable issue with respect to the present investigation is the fact that gradient-based identification criteria are generally inadequate for application on experimental data, such as instantaneous velocity fields measured with PIV. Due to the need for numerical differentiation measurement noise can severely contaminate the derivatives yielding less reliable vortex core

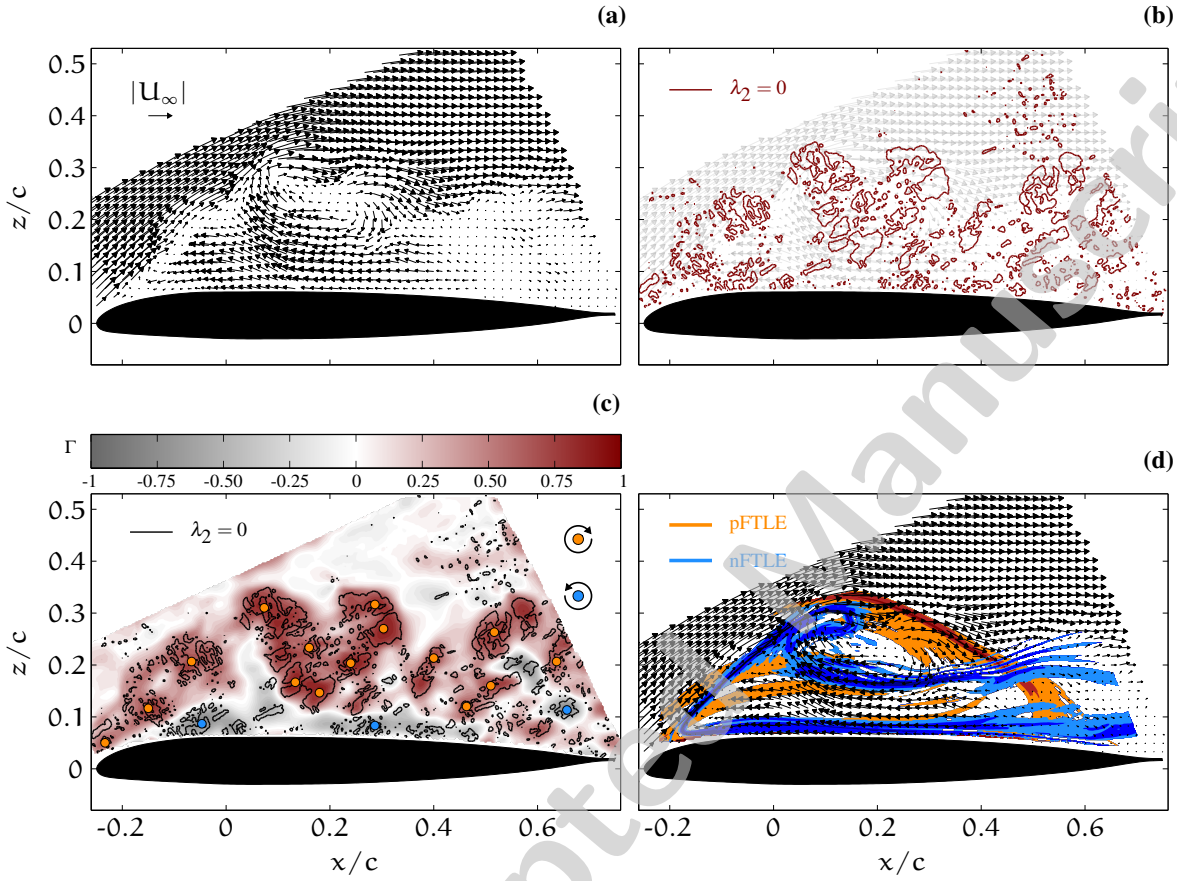

Fig. 1 a The instantaneous velocity field at $\alpha = 26.8°$ on the upstroke ($\alpha_0 = 20°$, $\alpha_1 = 8°$, $k = 0.050$); Eulerian vortex detection: **b** the corresponding zero contour lines of λ_2 and **c** a combined representation of the scalar field Γ (colour-coded) and the zero contour lines of λ_2, the markers indicate the location of (•) clockwise and (•) anticlockwise rotating vortices determined by the Γ-criterion; **d** Lagrangian coherent structures indicated by the ridges in the pFTLE and nFTLE fields.

identification. This is elucidated in figure 1 for the λ_2-criterion[1]. The conjecture made by Jeong and Hussain states that vortex cores are regions where $\lambda_2 < 0$. Hence, the presence and location of vortical structures in the instantaneous velocity field depicted in figure 1**a** is revealed by the zero contour lines of λ_2 (see figure 1**b**). Although the λ_2-identification scheme seems able to discern single structures in the shear zone between the viscous separated flow region and the inviscid external flow, it does neither allow to pinpoint the individual vortex axes nor to determine the geometry of the various vortex cores. This clearly reveals the need for an alternative, preferably non-local, Galilean invariant procedure which does not require the computation of derivatives. The alternative solution that was adopted here is based on a two-dimensional form of the dimensionless scalar function Γ that was first introduced by Michard et al. (1997). The function is derived directly from the two-dimensional in-plane velocity field and is defined in discrete form as

$$\Gamma(\mathbf{x}_i) = \frac{1}{M} \sum_{\mathbf{x}_j \in S_i} \frac{[(\mathbf{x}_j - \mathbf{x}_i) \times (\mathbf{u}_j - \tilde{\mathbf{u}}_i)] \cdot \mathbf{n}}{|\mathbf{x}_j - \mathbf{x}_i| \cdot |\mathbf{u}_j - \tilde{\mathbf{u}}_i|} = \frac{1}{M} \sum_{\mathbf{x}_j \in S_i} \sin(\theta_{ij}) \quad , \tag{1}$$

[1]The results obtained by the Q- , Δ- and λ_2-criteria overlap to a great extent for the present case, hence only the λ_2 results are presented.

with S_i a two-dimensional area around $\mathbf{x}_i$, M the number of grid points $\mathbf{x}_j$ inside S_i with $j \neq i$, $\mathbf{n}$ the unit normal vector, $\mathbf{u}_j$ the velocity at $\mathbf{x}_j$, $\tilde{\mathbf{u}}_i$ the local mean velocity around $\mathbf{x}_i$, and θ_{ij} the angle formed by the vectors $\mathbf{x}_j - \mathbf{x}_i$ and $\mathbf{u}_j - \tilde{\mathbf{u}}_i$. The local mean velocity is taken into account in order for Γ to be Galilean invariant (cf. Graftieaux et al. (2001)).

According to its definition, Γ is a dimensionless scalar function, with $-1 \leq \Gamma \leq 1$. The location of possible vortex axes is indicated by the local extrema of Γ and the sense of rotation is given by the sign of the local extremum. The distribution of $\Gamma(\mathbf{x})$ has been computed for the instantaneous velocity field depicted in figure 1**a** and is colour-coded in figure 1**c**, where the markers indicate the assessed vortex axes locations, i. e. (●) for clockwise and (●) for anticlockwise rotating vortices. The zero contour line of λ_2 allows for the validation of the detected vortex centres.

Besides the detection of the location of the vortex centres, their trajectories over a time series of flow fields have been traced. For this purpose, the convection velocity of the individual identified vortex centres within the reference frame are used to predict their future position and narrow the number of possible follow-up vortices. The tracing of the trajectories allows for the investigation of the spatiotemporal evolution of the vortical structures.

3.2 Lagrangian Approach

Alternatively to the routinely used Eulerian methods, some coherent structure identification algorithms that are Lagrangian in nature have been introduced into the fluid dynamics community during the last decades (cf. Peacock and Dabiri (2010) and references therein). The Lagrangian approach leverages the properties of fluid particle trajectories for the identification of coherent structures. Hence, they are inherently objective, they include information on the history of the flow, and they have a clear physical interpretation. The most popular Lagrangian approach, which was adopted in the present study, leverages finite-time Lyapunov exponents (FTLEs) and was introduced by Haller and Yuan (2000).

The FTLE method reverts directly to the fluid particle trajectories and is therefore inherently objective. The particle trajectories can be integrated in forward as well as in backward time yielding positive finite-time Lyapunov exponent (pFLTE) and negative finite-time Lyapunov exponent (nFTLE) fields. The ridges in the pFTLE field reveal material lines normal to which fluid particles are being stretched or repelled, consequentially they are referred to as repelling material lines or stable manifolds. Vice versa, ridges in nFTLE fields visualise attracting materials or unstable manifolds, i. e. lines along which fluid particles are being elongated, when integrating the trajectories in backward time. The flow field around the intersection of a repelling and an attracting material line resembles that of a saddle point. Moreover, when attached to a solid surface attracting material lines depict separation lines while attachment lines are repelling material lines. This FTLE method thus yields candidate material lines and captures features of the flow that are familiar from flow visualisation experiments. According to Shadden et al. (2005) the ridges in the FTLE fields delineate regions that exhibit qualitatively different dynamical behaviour, hence indicated the boundaries of Lagrangian coherent structures (LCSs). For a comprehensive discussion of the general properties and basic concepts involved in the computation of the FTLE, the reader is referred to i. a. Haller (2001, 2002); Shadden et al. (2005); and Garth et al. (2007).

The presence and form of the relevant LCSs corresponding to the previously presented instantaneous velocity field are indicated in figure 1**d** by the ridges in the pFTLE and nFTLE fields that are blank for values less than 30 % of the maximum of the field. The FTLE-fields presented and discussed in the course of this paper have been computed utilising the software package *ManGen*, a toolset for analysing dynamical systems, originally created at the California Institute of Technology by Lekien and Coulliette. In an attempt to filter and smoothen the data set prior to the Lagrangian analysis, a

low-order POD reconstruction is adopted. Based on the basic properties of the POD, the application of the FTLE method on a set of low-order reconstructed fields allows to focus on the behaviour of the large-scale coherent structures that dominated the motion. All FTLE-fields depicted here have been calculated based on the low-order POD reconstruction of the velocity field retaining the first 10 modes.

3.3 Proper Orthogonal Decomposition

A third alternative approach to extract salient flow structures is based on a POD procedure. Akin to the previously discussed Lyapunov exponents, the principle of the POD originates from dynamical systems and bifurcation theory. The POD method denotes a procedure for finding a basis of orthogonal spatial and temporal functions for a modal bi-orthogonal decomposition from an ensemble of spatiotemporal signals. The fundamental idea is to represent the random spatiotemporal signal as a series of the deterministic spatial functions with the temporal functions as random coefficients such that the original signal is approximated as accurate as possible based on an energy-weighted measure.

With regard to the present investigation, the two-dimensional in-plane velocity field $\mathbf{u} = (u, w)$ was decomposed according to

$$\mathbf{u}(x, z, t_\mathrm{n}) = \sum_{i=1}^{N} a_\mathrm{i}(t_\mathrm{n})\ \psi_\mathrm{i}(x, z) \quad , \tag{2}$$

where N is the number of instantaneous field realisations and t_n is the discrete time stamp. According to Lumley (1970), every spatial function or mode $\psi_\mathrm{i}(x,z)$ can be associated with an instantaneous organised flow pattern whose temporal evolution is described by the corresponding temporal mode $a_\mathrm{i}(t)$. Thus, the POD yields a systematic mathematical tool to define and identify coherent structures in a complex flow system as well as to study their spatiotemporal evolution. The practical implementation is based on the snapshot method introduced by Sirovich (1987). More details on the mathematical framework and methodology of the POD method can be found in i. a. Lumley (1970); Sirovich (1987); and Aubry et al. (1991).

4 Results and Discussion

Analogous to the classification of Shih et al. (1992) with regard to the flow over an airfoil pitching-up at constant rate, the unsteady flow development over an oscillation airfoil can be divided into five different stages. With the starting point of a cycle taken at the minimum incidence angle, the flow will consecutively pass through the following stages within each individual cycle: 1) the *attached flow stage*; 2) the *stall development stage*; 3) *stall onset*; 4) the *stalled stage*; and 5) *flow reattachment*. Based on the complementary information of the different coherent structures identification methods a deeper insight can be provided into the spatiotemporal evolution of vortical structures within a single dynamic stall life cycle. First, a general description of the dynamic phenomena within a single dynamic stall life cycle is outlined. In a second part the onset of dynamic stall is specified directly from the velocity field data.

4.1 Dynamic Stall Life Cycle

Attempting a general description of the characteristic features of the dynamic stall life cycle, the velocity field data and surface pressure distributions acquired within a sole harmonic oscillation specified by $\alpha_0 = 20°$, $\alpha_1 = 8°$, and $k = 0.10$ are regarded. The typical dynamic stall curves of the lift

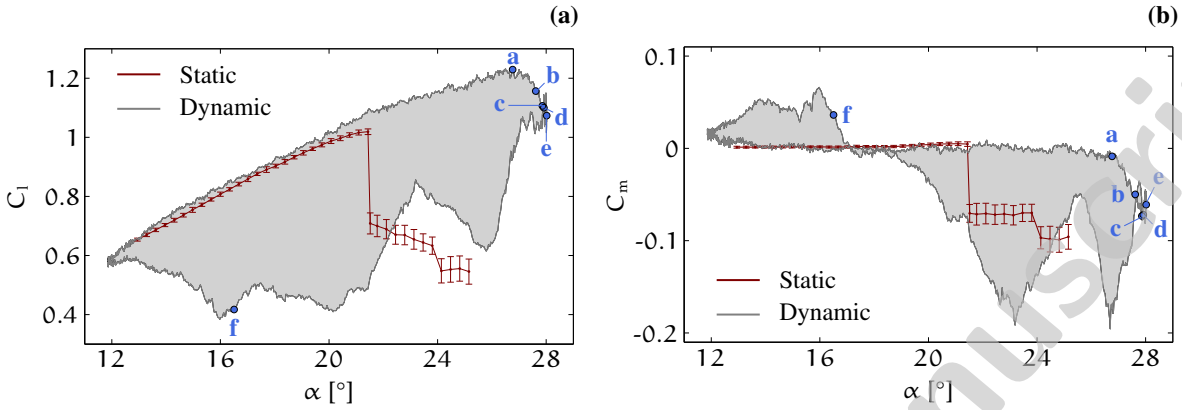

Fig. 2 Static and dynamics airloads in function of angle of attack: **a** lift and **b** pitching moment coefficient ($\alpha_0 = 20°$, $\alpha_1 = 8°$, $k = 0.10$).

and pitching moment coefficients are depicted in figure 2. Additionally, the response of the aerodynamic load coefficients in absence of dynamic effects is presented, revealing a static stall angle of attack $\alpha_{ss} = 21.4°$. The error bars indicate the standard deviation of the aerodynamic load coefficients during the period of measurement for the various static angles of incidence. The markers on the dynamical stall curves – that can be recognised by the strong hysteresis effects – indicate selected points for which the instantaneous velocity fields and surface pressure distributions are depicted in figure 3. Here, only every sixth velocity vector is shown for the sake of visibility and the dimensionless out-of-plane component of the vorticity is colour-coded. The dots indicate the locations of clockwise and anticlockwise rotating vortices determined by the Eulerian detection algorithm.

During the first part of the cycle, i. e. from the minimum incidence angle upstroke to the static stall angle, the flow is attached to the airfoil's surface and the surface pressure distribution exhibits an increasing suction peak near the leading edge. Furthermore, the lift increases linearly with the angle of incidence at a rate approximately equal to its static counterpart. Increasing the angle of attack beyond the static stall angle, an adverse pressure gradient builds up downstream of the leading edge eliciting the development of a recirculating flow on the airfoil's suction side. Between this region of flow reversal and the free stream flow a shear layer forms. Shortly after its development, the shear layer is subjected a primary instability (cf. Ho and Huerre (1984)) as a result of which the initially contained vorticity is redistributed into separate lumped vortices (figure 3**a**). At first, these small-scale regularly spaced shear layer vortices – which are all clockwise rotating – are convected downsteam by the external flow and interact only weakly with each other. Meanwhile, the suction peak continues to rise. Consequentially, the lift force continuously increases as well, although with a slightly different slope than below the static stall angle. The latter is due to the reversing flow layer extending over a considerable part of the airfoil's chord. Hence, despite the occurrence of flow reversal, the external flow is only mildly deviated while the aerodynamic lift keeps augmenting. This differs significantly from the observations of the flow over a stationary airfoil, where flow reversal elicits massive flow separation accompanied by a dramatic decrease of the lift and pitching moment. However, the small-scale vortices in figure 3**a** do not remain this way for long but evolve very quickly. As a result of a secondary instability of the shear layer they merge into larger structures (see figure 3**b**). Eventually this leads to the formation of one large-scale vortical structure which is referred to as the primary dynamic stall vortex (figure 3**c**). This dynamic stall vortex thus consists of a combination of the rolled-up shear layer and the remnants of several vortices generated by the instability of the shear layer. During its formation the dynamic stall vortex remains temporarily in place before it breaks away from the airfoil's surface. The presence of the large-scale structure can

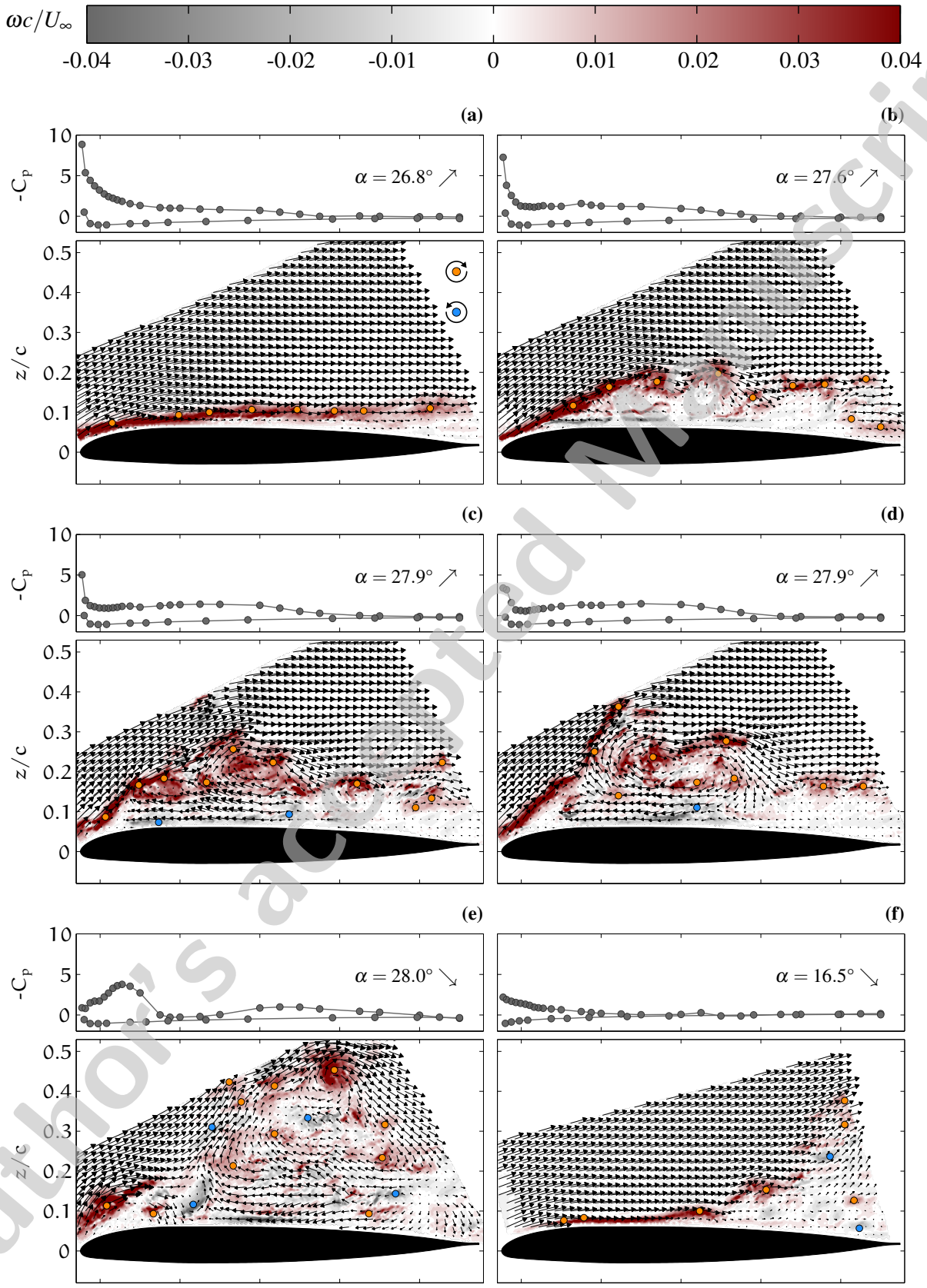

Fig. 3 Instantaneous flow fields with detected vortex cores: (●) clockwise and (●) anticlockwise rotating; and the respective surface pressure distribution for the states marked in figure 2 within a single oscillation ($\alpha_0 = 20°$, $\alpha_1 = 8°$, and $k = 0.10$).

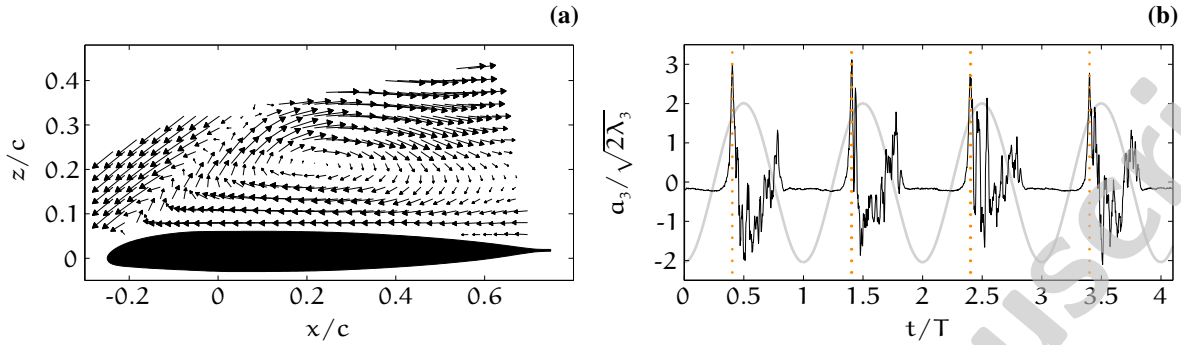

Fig. 4 From the POD of the ensemble of velocity fields $\mathbf{u} = (u, w)$: **a** the third spatial mode $\psi_3(x, z)$ and **b** the corresponding time development coefficient $a_3(t)$ ($\alpha_0 = 20°$, $\alpha_1 = 8°$, $k = 0.050$).

be recognised by a plateau in the surface pressure distribution between approximately $x = -0.1\,c$ and $x = 0.2\,c$ on the suction side (figure 3**c**-**d**). As a result of the strong interaction between between the dynamic stall vortex and the reversing flow near the airfoil's surface counter-rotating vortices emerge in that region (figure 3**d**). These anticlockwise rotating structures move towards the leading edge and push the primary stall vortex away from the surface. The detachment of the primary stall vortex from the boundary layer that provides its circulation marks the *dynamic stall onset*, and consequentially the end of the *stall development stage* and the beginning of the *stalled stage*. With the primary stall vortex living its life, additional circulation accumulates upstream of it, leading to the formation of a secondary stall vortex. These primary originating vortices detach in close succession and are simultaneously convected downstream. During the convection process the flow can briefly follow the nose again. The massive flow separation downstream of approximately $x = 0.1\,c$ slows down free stream flow and thus the convection of vorticity from the leading edge. This results in the formation of a leading edge recirculation region which is confined by a shear layer containing the accumulated vorticity (figure 3**e**). While this recirculation region grows and moves slowly downstream the confining shear layer rolls up to form anew a large-scale coherent structure. This process of vortex formation and detachment is repeatedly observed during downstroke. The large-scale vortex shedding and the associated large fluctuations of the aerodynamic load coefficients characterise the *stalled stage*. It continues until the flow is able to reattach near the end of the downstroke (figure 3**f**). Finally, *flow reattachment* allows for the aerodynamic loads to return to their initial un-stalled values.

The succession of events qualitatively elucidated above, is qualitatively observed for the entire parameter span relevant to this study. Hence, it is deemed to adequately cover the prominent events of the dynamic stall process for the prevailing flow conditions and chosen airfoil profile.

4.2 Dynamic Stall Onset

The prominent feature of the stall development stage is the formation and growth of a large-scale dynamic stall vortex. The dynamic stall vortex will temporarily resides above the airfoil's surface before it is being pinched off as a result of a vortex induced separation process (cf. (Peridier et al., 1991; Obabko and Cassel, 2002)). The dynamic stall onset is defined in this work as the detachment[2] of the primary stall vortex and is determined from the experimental data based on the POD of the two-component velocity field $\mathbf{u} = (u, w)$ according to equation 2. The spatial modes respective the velocity decomposition are denoted by $\psi_i(x, z)$ and their relative energy contribution is indicated by

[2]According to the terminology adopted here vortex separation or detachment refers to the situation where a vortex lifts off the airfoil and is convected downstream by the free stream flow. It should not be confused with flow separation.

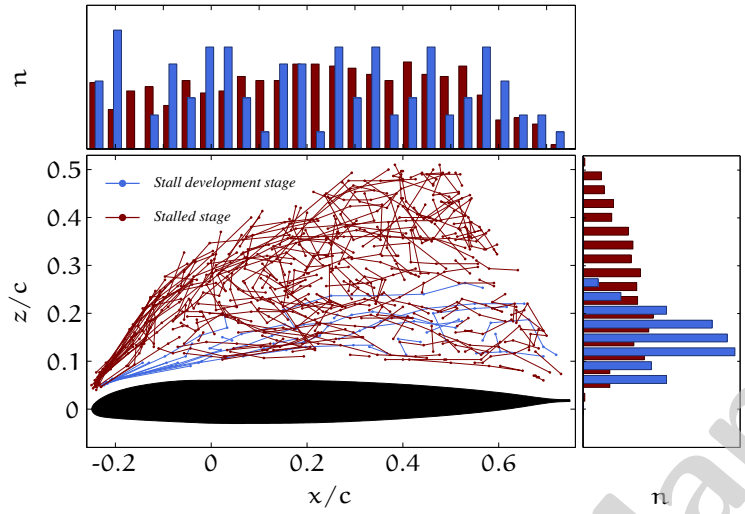

Fig. 5 Trajectories of positive vortices emerging before and the after stall onset. The histograms depict the probability density functions of the horizontal and vertical location of the vortex centres respective the different stages.

the time development coefficients $a_i(t)$.

The first and second mode respectively represent a fully attached and a fully separated flow state. However, the most interesting mode with regard to the stall onset is the third spatial mode (see figure 4a). This mode can be interpreted as a large-scale coherent structure or dynamic stall vortex, an idea that is supported by the temporal development of the coefficient $a_3(t)$ (figure 4b). During the first part of the cycle the flow is attached and the magnitude of $a_3(t)$ is small and approximately constant (the airfoil's oscillating motion is drawn auxiliary). Hence, the contribution of ψ_3 to the decomposition is inconsiderable and only gains in importance near the end of the upstroke motion when the primary stall vortex is being formed. This primary large-scale structure dominates the flow field until it is being pinched off from the separated boundary layer that provides its circulation. Consequentely, it is expected that the weight of the third mode attains a local maximum shortly before the detachment of the primary stall vortex, i. e. stall onset. The angle of attack at this local maximum is referred to as the dynamic stall onset angle of attack and is denoted by α_{ds}.

The fact that the POD based assignment of the stall onset actually corresponds to an invasive topological change was verified by a Lagrangian coherent structure analysis. The LCSs for four instantaneous subsequent velocity fields shortly after dynamic stall onset are depicted in figure 6. The flow field around the intersection of a repelling and an attracting material line, visualised by ridges in the pFTLE and nFTLE fields respectively, resembles that of a saddle point. The black circles mark the approximate location of the saddle point at the boundary of the stall vortex. This saddle point moves in time and indicates the detachment of the vortex from the boundary layer, which marks the end of the stall development stage.

Furthermore, comparison of the trajectories of the detected vortices, emerging before and after the assessed stall onset confirms that this is indeed a turning point. A subtle but significant change can be recognised in the orientation of the trajectories of the vortices that originate at the very leading edge for angles of attack before and beyond α_{ds} (see figure 5).

It should be noted that the POD only defines a mathematical framework and special care is required when interpreting the results and associating the spatial modes with coherent structures. Nevertheless, due to the congruence with the Eulerian and Lagrangian picture, the POD method is found to be very useful and reliable in defining the dynamic stall onset in the present context.

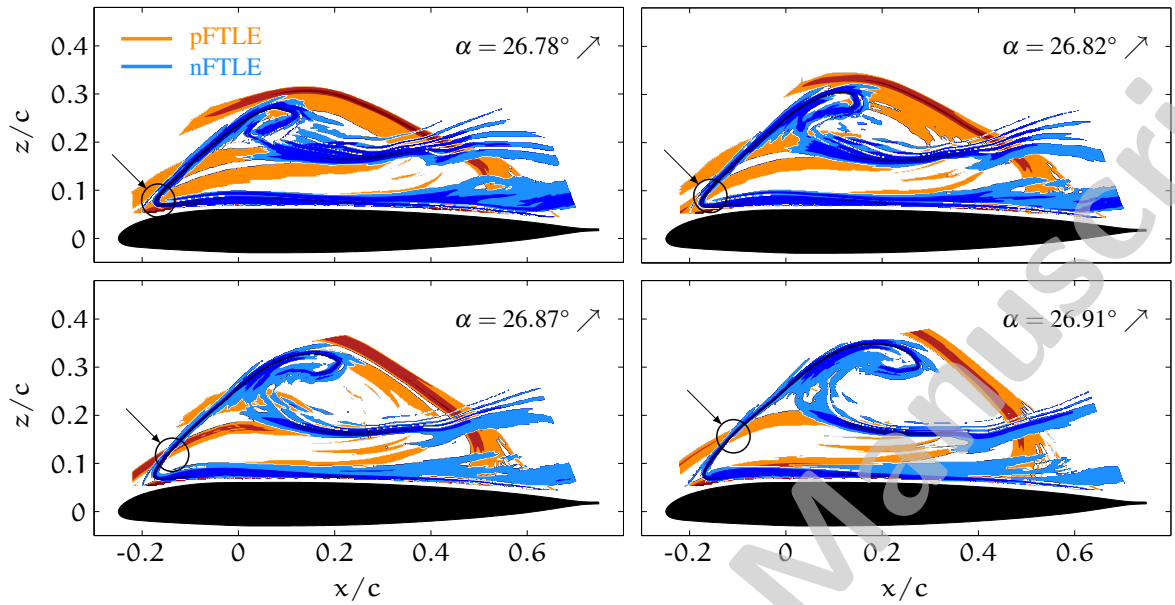

Fig. 6 Flow field topology shortly after dynamic stall onset as indicated by the LCSs recognised by the ridges in the pFTLE and nFTLE fields. The black circles marks the approximate position of the saddle point ($\alpha_0 = 20°$, $\alpha_1 = 8°$, $k = 0.05$).

5 Conclusion and Perspectives

Time-resolved velocity field information and unsteady surface pressure distributions were gathered during wind tunnel experiments and elaborated by an extensive coherent structure analysis. The characteristic features of the unsteady flow field were identified and analysed utilising different coherent structure identification methods. The combination of time-resolved imaging and an extensive coherent structure analysis provided new insights in the complex dynamic stall process and yielded a better understanding of the succession of fluid dynamic events within a single dynamic stall life cycle. The dynamic stall onset was identified as a result of a vortex induced separation and was specified directly from the velocity field.

Due to the inherent unsteady nature of the dynamic stall process, the time-resolved approach has to be regarded the preferential approach. Continuing on this avenue of investigation, the objectives of future research are: characterising the associated delay with respect to static stall; identifying the influence of the airfoil's motion parameters on the stall delay; and determining the causality between the passage of coherent motion in the separated flow region and fluctuations of the aerodynamic load coefficients.

Acknowledgements The authors thank H. Mai, T. Büte, J. Nuhn and A. Henning for their contribution to the wind tunnel measurements.

References

Aubry N, Guyonnet R, Lima R (1991) Spatiotemporal analysis of complex signals: Theory and applications. J Stat Phys 64:683–739

Carr L (1988) Progress in analysis and prediction of dynamic stall. J Aircraft 25(1):6–17

Carr L, McAlister K, McCroskey W (1977) Analysis of the development of dynamic stall based on oscillating airfoil experiments. TN D-8382, NASA

Chong M, Perry A, Cantwell B (1990) A general classification of three-dimensional flow fields. Phys Fluids A: Fluid Dyn 2:765–777

Cucitore R, Quadrio M, Baron A (1999) On the effectivenss and limitations of local criteria for the identification of a vortex. Eur J Mech B Fluids 18(2):261–282

Degani A, Walker J, Smith F (1998) Unsteady separation past moving surfaces. J Fluid Mech 375:1–38

Doligalski T, Smith C, Walker J (1994) Vortex interactions with walls. Ann Rev Fluid Mech 26:573–616

Garth C, Gerhardt F, Tricoche X, Hagen H (2007) Efficient computation and visualization of coherent structures in fluid flow applications. IEEE Trans Visual Comput Graphics 13(6):1464–1471

Graftieaux L, Michard M, Grosjean N (2001) Combining PIV, POD and vortex identification algorithms for the study of unstready turbulent swirling flows. Meas Sci Technol 12:1422–1429

Haller G (2001) Distinguished material surfaces and coherent structures in three-dimensional fluid flows. Physica D 149:248–277

Haller G (2002) Lagrangian coherent structures from approximate velocity data. Phys Fluids 14(6):1851–1861

Haller G (2005) An objective definition of a vortex. J Fluid Mech 525:1–26

Haller G, Yuan G (2000) Lagragian coherent structures and mixing in two-dimensional turbulence. Physica D 147:352–370

Ho C, Huerre P (1984) Perturbed free shear layer. Ann Rev Fluid Mech 16:365–424

Hunt J, Wray A, Moin P (1988) Eddies, stream, and convergence zones in turbulent flows. In: Proceedings of the Summer Program 1988, N89-24555, pp 193–208

Jeong J, Hussain F (1995) On the identification of a vortex. J Fluid Mech 285:69–94

Lekien F, Coulliette C Mangen software package. URL `http://www.lekien.com/~francois/software/mangen/`

Lugt H (1979) Recent Developments in Theoretical and Experimental Fluid Dynamics, Springer, chap The Dilemma of Defining a Vortex, pp 309–321

Lumley J (1970) Stochastic Tools in Turbulence. Applied Mathematics and Mechanics - An International Series of Monographs 12, Academic Press

McAlister K, Carr L, McCroskey W (1978) Dynamic stall experiments on the NACA0012 airfoil. TP 1100, NASA

McCroskey W (1981) The phenomenon of dynamic stall. TM 81264, NASA

Michard M, Graftieaux L, Lollini L, Grosjean N (1997) Identification of vortical structures by a non local criterion - application to PIV measurements and DNS-LES results of turbulent rotating flows. In: Proceedings of the 11th Conference on Turbulent Shear Flows, Grenoble, France

Obabko A, Cassel K (2002) Detachement of the dynamic stall vortex above a moving surface. AIAA J 40(9):1811–1822

Peacock T, Dabiri J (2010) Introduction to focus issue: Lagrangian coherent structures. Chaos 20:1–3

Peridier V, Smith F, Walker J (1991) Vortex-induced boundary layer separation. part 1. the unsteady limit problem $Re \rightarrow \infty$. J Fluid Mech 232:99–131

Richard H, Bosbach J, Henning A, Raffel M, van der Wall B (2006) 2C and 3C PIV measurements on a rotor in hover condition. In: Proceedings of the 13th International Symposium on Applications of Laser Techniques to Fluid Mechanics, Lisbon, Portugal

Robinson S (1991) Coherent motions in the turbulent boundary layer. Ann Rev Fluid Mech 23:601–639

Shadden S, Lekien F, Marsden J (2005) Definition and properties of Lagrangian coherent structures from finite-time lyapunov exponents in two-dimensional aperiodic flows. Physica D 212:271–304

Shih C, Lourenco L, Van Dommelen L, Krothapalli A (1992) Unsteady flow past an airfoil pitching at constant rate. AIAA J 30(5):1153–1161

Sirovich L (1987) Turbulence and the dynamics of coherent structures; part I, II and III. Q Appl Math 45(3):561–590

Van Dommelen L, Cowley S (1980) On the Lagrangian description of unsteady boundary layer separation. part 1. general theory. J Fluid Mech 210:593–626